Anomalous Hall conductivity of noncollinear magnetic antiperovskites

Gautam Gurung, Ding-Fu Shao, Tula R. Paudel, and Evgeny Y. Tsymbal

Phys. Rev. Materials **3**, 044409 — Published 23 April 2019

DOI: 10.1103/PhysRevMaterials.3.044409

Anomalous Hall Conductivity of Non-Collinear Magnetic Antiperovskites

Gautam Gurung, Ding-Fu Shao,* Tula R. Paudel, and Evgeny Y. Tsymbal†

Department of Physics and Astronomy & Nebraska Center for Materials and Nanoscience, University of Nebraska, Lincoln, Nebraska 68588-0299, USA

The anomalous Hall effect (AHE) is a well-known fundamental property of ferromagnetic metals, commonly associated with the presence of a net magnetization. Recently, an AHE has been discovered in non-collinear antiferromagnetic (AFM) metals. Driven by non-vanishing Berry curvature of AFM materials with certain magnetic space group symmetry, anomalous Hall conductivity (AHC) is very sensitive to the specific type of magnetic ordering. Here, we investigate the appearance of AHC in antiperovskite materials family $ANMn_3$ (A = Ga, Sn, Ni), where different types of non-collinear magnetic ordering can emerge. Using symmetry analyses and first-principles density-functional theory calculations, we show that with almost identical band structure, the nearly degenerate non-collinear AFM Γ_{5g} and Γ_{4g} phases of $GaNMn_3$ have zero and finite AHC, respectively. In a non-collinear ferrimagnetic M-1 phase, $GaNMn_3$ exhibits a large AHC due to the presence of a sizable net magnetic moment. In the non-collinear antiperovskite magnets, transitions between different magnetic phases, exhibiting different AHC states, can be produced by doping, strain, or spin transfer torque, which makes these materials promising for novel spintronic applications.

I. Introduction

It is known that the anomalous Hall effect (AHE) emerges in metals with broken time-reversal symmetry (TRS) and strong spin-orbit coupling (SOC) [1]. Usually, the AHE is found in ferromagnetic (FM) metals, where a transverse voltage generated by a longitudinal charge current is sensitive to the net magnetization. The intrinsic AHE is driven by a fictitious magnetic field in the momentum space associated with the Berry curvature, a quantity inherent in the electronic band structure [2]. With the magnitude and direction determined by the magnetization and SOC, this fictitious magnetic field controls the charge current in a similar way as a real magnetic field in the ordinary Hall effect. The AHE vanishes in conventional collinear antiferromagnetic (AFM) metals due to the anomalous Hall conductivities being opposite in sign and hence cancelling each other for the two ferromagnetic sublattices with opposite magnetization. In other words, the existence of symmetry combining time reversal and lattice translation prohibits the AHE. This observation suggested that the presence of a non-vanishing net magnetic moment is the necessary condition to break the related symmetry and produce the AHE [3].

It appeared, however, that the AHE can be observed in certain types of non-collinear antiferromagnets, such as Mn_3X alloys (X = Ga, Ge, Ir, etc.) [4–8]. In these metals, the Mn moments are arranged in a Kagome-type lattice within the (111) plane. The magnetic space group symmetry operations in these compounds cannot eliminate the total Berry curvature, leading to a non-vanishing AHE [4]. The presence of a sizable AHE in non-collinear AFM metals is interesting for AFM spintronics, where an AFM order parameter, as a state variable, can be controlled on a much shorter time scale compared to magnetization in ferromagnets [9–11].

Importantly, specifics of magnetic ordering in non-collinear AFM materials associated with different magnetic space group symmetries have a strong impact on the AHE [12, 13]. For example, it was found that the AHC tensors have a different form in Mn_3X (X = Ga, Ge, and Sn) and Mn_3Y (Y = Rh, Ir, and Pt) compounds, due to different magnetic moment configurations. One can expect therefore that a significant change in the anomalous Hall conductivity (AHC) can emerge at the magnetic phase transition associated with switching between different non-collinear magnetic orderings. Realizing such an effect in practice would be interesting for potential spintronic applications, and therefore exploring the AHE in possible material systems with competing and tunable non-collinear magnetic phases is valuable.

Antiperovskite materials are potential candidates for the control of the AHE by tunable non-collinear magnetism. Antiperovskites have a perovskite structure, where cation and anion positions are interchanged [Fig. 1(a)]. Abundant functional properties have been discovered in these materials, such as superconductivity [14], magnetoresistance [15], and magnetovolume [16 – 18], magnetocaloric [19 , 20], and barocaloric [21] effects. Manganese nitride antiperovskites $ANMn_3$ (A = Ga, Cu, Ni, etc.) are typically metallic and often reveal complex magnetic orderings [16, 22 , 23]. Various magnetic phases, such as non-collinear AFM Γ_{5g} and Γ_{4g} phases and a non-collinear ferrimagnetic M-1 phase have been found in these compounds [Fig. 1]. Transformations between these magnetic phases can be induced by perturbations, such as doping, pressure, and temperature [23–25]. It has also been predicted that the transition between the Γ_{5g} and Γ_{4g} phases can be achieved using a spin transfer torque [26]. These properties make $ANMn_3$ compounds promising for a functional control of the non-

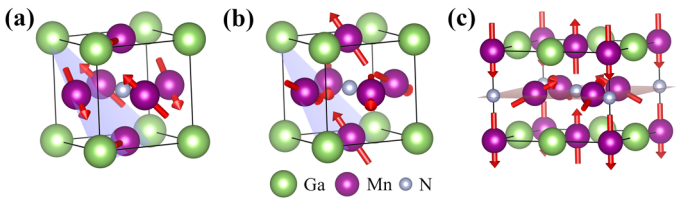

FIG. 1. Different non-collinear magnetic phases in AFM antiperovskite $GaNMn_3$: (a) Γ_{5g}, (b) Γ_{4g}, and (c) M-1. Red arrows denote magnetic moments.

collinear magnetism and thus interesting for exploring the AHE in different magnetic phases.

In this paper, we consider gallium manganese nitride $GaNMn_3$ as a representative antiperovskite material to investigate the magnetic phase dependent AHC of the whole $ANMn_3$ family. The high temperature paramagnetic phase of $GaNMn_3$ has a cubic crystal structure with the space group $Pm\bar{3}m$. The Γ_{5g} phase emerges below room temperature [Fig. 1(a)] and represents the most common non-collinear AFM phase of the $ANMn_3$ compounds. In this phase, to avoid the frustration from the triangular geometry of the Ga-Mn Kagome-type lattice in the (111) plane, the magnetic moments of the three Mn atoms form a chiral configuration with the 120° angle between each other. The Γ_{4g} magnetic structure is another common non-collinear AFM phase in the $ANMn_3$ family, which can be obtained from the Γ_{5g} phase by rotating all magnetic moments around the [111] axis by 90° [Fig. 1(b)]. Both the Γ_{5g} and Γ_{4g} phases have zero net magnetization. $GaNMn_3$ also exhibits a non-collinear ferrimagnetic M-1 phase [Fig. 1(c)], which can be stabilized by stoichiometric deficiency or high pressure [23]. In this phase, the Mn magnetic moments are antiferromagnetically (ferromagnetically) coupled in (between) the Ga-Mn (001) planes, resulting in collinear AFM sublattices within these planes. On the other hand, the magnetic moments in the Mn-N (002) planes are arranged non-collinearly (Fig. 1(c)), leading to the net magnetic moment along the [001] direction.

Using symmetry analyses and first-principles density-functional theory (DFT) calculations, we explore the AHE of the three non-collinear magnetic phases of $GaNMn_3$. We show that with nearly identical band structure, the nearly degenerate AFM Γ_{5g} and Γ_{4g} phases have zero and finite AHC, respectively. A similar behavior is exhibited by non-collinear antiferromagnetic antiperovskites $SnNMn_3$ and $NiNMn_3$. In a non-collinear ferrimagnetic M-1 phase, $GaNMn_3$ exhibits a large AHC due to the presence of a sizeable net magnetization. With a possibility to control the appearance of these magnetic phases by external stimulus, the predicted variation of the AHC between different magnetic phases in the same material point to a new approach of designing the AHE-based functional devices for spintronic applications.

II. Symmetry analysis

Within the linear response theory, the intrinsic AHC is expressed as the integral of the total Berry curvature ($\Omega_{\alpha\beta}$) over the Brillouin zone (BZ) of the crystal [1, 27]

$$\sigma_{\alpha\beta} = -\frac{e^2}{\hbar}\int_{BZ}\frac{d^3\vec{k}}{(2\pi)^3}\Omega_{\alpha\beta}(\vec{k}), \quad (1)$$

where the total Berry curvature $\Omega_{\alpha\beta} = \sum_n f_n(\vec{k})\Omega_n^{\gamma}(\vec{k})$ is the sum of the Berry curvatures $\Omega_{n,\alpha\beta}(\vec{k})$ corresponding the individual bands n, $f_n(\vec{k})$ is the Fermi distribution function, and indices (α, β) denote Cartesian co-ordinates. The expression for the Berry curvature $\Omega_{n,\alpha\beta}(\vec{k})$ is given by [1, 27]

$$\Omega_{n,\alpha\beta}(\vec{k}) = -2i\hbar^2\sum_{m\neq n}\frac{\langle\psi_{n,\vec{k}}|v_\alpha|\psi_{m,\vec{k}}\rangle\langle\psi_{m,\vec{k}}|v_\beta|\psi_{n,\vec{k}}\rangle}{(E_m(\vec{k})-E_n(\vec{k}))^2}, \quad (2)$$

where $\psi_{n,\vec{k}}$ is the Bloch function and $\vec{v}$ is the velocity operator. Space group symmetry of a material determines the presence or absence of a finite AHC. For example, since $\Omega_{n,\alpha\beta}(\vec{k})$ is odd with respect to time reversal symmetry, i.e. $\Omega_{n,\alpha\beta}(-\vec{k}) = -\Omega_{n,\alpha\beta}(\vec{k})$, the total Berry curvature $\Omega_{\alpha\beta}$ and hence the AHC are zero for non-magnetic materials. Similarly, if there is symmetry operation $\hat{O}$ transforming $\vec{k}$ to $\vec{k}'$ (i.e., $\vec{k}' = \hat{O}\vec{k}$), such as two-fold rotation or mirror reflection, for which $\hat{O}\Omega_n(\vec{k}') = -\Omega_n(\vec{k})$, the AHC vanishes [12, 13]. In non-collinear AFM materials, such as $GaNMn_3$, various magnetic phases are associated with different magnetic space group symmetries (TABLE I), resulting in different AHC.

The Γ_{5g} phase of $GaNMn_3$ is characterized by a lattice of magnetic "whirls" composed of non-collinear Mn magnetic moments in the (111) plane [Fig. 2(a)]. This arrangement forms the magnetic space group $R\bar{3}m$, which has three mirrors planes perpendicular to the (111) plane. Mirror symmetry M preserves the spin component perpendicular to the mirror plane and reverses the spin components parallel to the mirror plane. As shown in Fig. 2(a), the magnetic moments of the Mn atoms at the mirror planes (indicated by the dashed lines in Fig. 2(a)) are always perpendicular to this plane. Therefore, application of the symmetry transformations $M = M_{0\bar{1}1}$, $M_{10\bar{1}}$, or $M_{\bar{1}10}$ preserves the original configuration of magnetic moments. The invariance under these three mirror symmetry transformations causes the AHE in the Γ_{5g} phase to vanish. For example, under the $M_{\bar{1}10}$ symmetry operation, the Berry curvature is transformed as $M_{\bar{1}10}\Omega_{xy}(k_y, k_x, k_z) = -\Omega_{xy}(k_x, k_y, k_z)$, which implies that the integral over the whole Brillouin zone in Eq. (1) leads to a zero σ_{xy}. Similarly, Ω_{yz} and Ω_{zx} are odd with

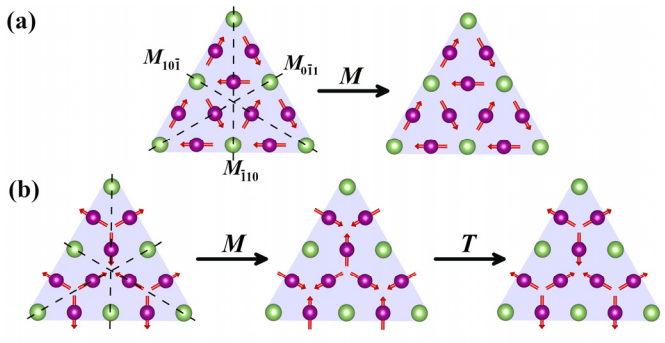

FIG. 2. Symmetry operations for non-collinear AFM phases Γ_{5g} (a) and Γ_{4g} (b) in the (111) Ga-Mn plane of $GaNMn_3$. (a) The Γ_{5g} phase preserves mirror planes $(\bar{1}10)$, $(10\bar{1})$ and $(0\bar{1}1)$ (denoted by dashed lines) and is invariant under symmetry transformations $M = M_{0\bar{1}1}, M_{10\bar{1}}$ or $M_{\bar{1}10}$. (b) The Γ_{4g} phase does not preserve the mirror planes, but is invariant under the product of mirror symmetry M and time reversal symmetry T. Red arrows denote the magnetic moments. Dotted lines denote the mirror planes.

respect to $M_{0\bar{1}1}$ and $M_{10\bar{1}}$, respectively. Table IV in Appendix B shows details of different symmtry transfromations.

This odd property of the Berry curvature in $GaNMn_3$ under the mirror symmetry transformations is broken in the Γ_{4g} phase. In this phase, the Mn magnetic moments form a lattice of "vertices" in the (111) plane, in which the magnetic moments of the Mn atoms within the mirror plane are parallel to this plane [Fig. 2(b)]. This configuration corresponds to the magnetic space group $R\bar{3}m'$, in which the mirror symmetries are broken. As seen from Fig. 2(b), mirror symmetry transformation M reverses all the magnetic moments.

In contrast, the product of mirror symmetry M and time reversal symmetry T is preserved in the Γ_{4g} phase. As shown in Fig. 2(b), when reversal of all moments by the mirror symmetry operation M is followed by the time reversal symmetry transformation T all the moments are reversed back to their initial configuration. The presence of the combined TM symmetry makes the Berry curvature an even function of wave vector $\vec{k}$. For example, applying the $TM_{\bar{1}10}$ transformation we obtain $TM_{\bar{1}10}\Omega_{xy}(k_y, k_x, k_z) = \Omega_{xy}(-k_x, -k_y, -k_z)$. This even property of the Berry curvature with respect to $TM_{\bar{1}10}$, $TM_{[0\bar{1}1]}$, and $TM_{[10\bar{1}]}$ makes the AHC non-zero in the Γ_{4g} phase. The complete analysis of the TM symmetry transformations is given in Table IV (Appendix B).

Magnetic space group symmetry determines the shape of the AHC tensor. While in the Γ_{5g} phase, all the nine components of the AHC tensor are zero, in the Γ_{4g} phase, corresponding to the magnetic space group $R\bar{3}m'$, the AHC tensor is non-zero. TABLE I shows that there are six non-vanishing matrix elements

TABLE I. Matrix elements of the AHC tensor for different magnetic phases in $GaNMn_3$. Here, the ordinary Cartesian coordinates are used, i.e. $\hat{x}||[100]$, $\hat{y}||[010]$, and $\hat{z}||[001]$.

Magnetic Phase	Γ_{5g}	Γ_{4g}	M-1
Magnetic Space Group	$R\bar{3}m$	$R\bar{3}m'$	P4
AHC tensor	$\begin{bmatrix} 0 & 0 & 0 \\ 0 & 0 & 0 \\ 0 & 0 & 0 \end{bmatrix}$	$\begin{bmatrix} 0 & \sigma_{xy} & -\sigma_{xy} \\ -\sigma_{xy} & 0 & \sigma_{xy} \\ \sigma_{xy} & -\sigma_{xy} & 0 \end{bmatrix}$	$\begin{bmatrix} 0 & \sigma_{xy} & 0 \\ -\sigma_{xy} & 0 & 0 \\ 0 & 0 & 0 \end{bmatrix}$

of the AHC tensor in the Γ_{4g} phase with only one σ_{xy} being independent.

In the non-collinear ferrimagnetic M-1 phase, the unit cell is a tetragonal $\sqrt{2} \times \sqrt{2} \times 1$ supercell of the conventional cubic unit cell without any distortion [Fig. 1 (c)]. In this phase, $GaNMn_3$ has a net magnetization along the [001] direction. Therefore, a non-zero AHC is expected in this case similar to that in ferromagnetic metals. TABLE I shows the AHC tensor for the magnetic space group symmetry P4 corresponding to the M-1 phase. Like in collinear ferromagnetic metals, the AHC tensor has two non-zero components with only one σ_{xy} being independent.

III. Methods

Next, we perform first-principles DFT calculations to obtain the AHC of the three non-collinear magnetic phases of $GaNMn_3$. The DFT calculations are performed using a plane-wave pseudopotential method with the fully-relativistic ultrasoft pseudopotentials [28] implemented in Quantum-ESPRESSO [29]. The exchange and correlation effects are treated within the generalized gradient approximation (GGA) [30]. We use the plane-wave cut-off energy of 52 Ry, the charge density cut-off energy of 520 Ry, and the k-point mesh of 16 × 16 × 16 for the cubic Γ_{5g} and Γ_{4g} phases and 12 × 12 × 16 for the tetragonal M-1 phase in $GaNMn_3$. Spin-orbit coupling is included in all the calculations. The electronic structure is converged to 10^{-7} eV/cell. The lattice parameters are obtained by fitting the calculated total energy to the Murnaghan equation of state [31].

The AHC is calculated using the PAOFLOW code [32] based on pseudo-atomic orbitals (PAO) [33,34]. Tight-binding Hamiltonians are constructed from the non-self-consistent DFT calculations with a 16 × 16 × 16 k-point mesh for the Γ_{5g} and Γ_{4g} phases and a 12 × 12 × 16 k-point mesh for the M-1 phase. Then, the AHC are calculated with a 48 × 48 × 48 k-point mesh for the Γ_{5g} and Γ_{4g} phases and a 46 × 46 × 48 k-point mesh for the M-1 phase using the adaptive broadening method. We find

TABLE II. Calculated lattice parameters a and AHC σ_{xy} for different magnetic phases of $ANMn_3$ (A = Ga, Ni, Sn).

	a (Å)			σ_{xy} ($\Omega^{-1}cm^{-1}$)		
$ANMn_3$	Γ_{5g}	Γ_{4g}	M-1	Γ_{5g}	Γ_{4g}	M-1
$GaNMn_3$	3.87	3.87	3.82	0	40	377
$NiNMn_3$	3.84	3.84	-	0	130	-
$SnNMn_3$	3.99	3.99	-	0	133	-

satisfactory convergence of the calculated AHC for a k-mesh of denser than 40×40×40. Increasing the grid size to 100×100×100 changed the AHC negligibly.

The symmetry determined geometries of the AHC tensor are obtained using the FINDSYM code and the linear response symmetry code [35]. The figures are created using VESTA [36] and gnuplot [37].

IV. Results

The calculated lattice parameters of $GaNMn_3$ in different magnetic phases are listed in TABLE II. For the Γ_{5g} phase of $GaNMn_3$, we find a = 3.869 Å, which is close to the experimental and previously calculated values [22, 23, 38, 39, 40], and is identical to the calculated lattice parameter of Γ_{4g}. The calculated lattice parameter of the M-1 phase is smaller, which is consistent with the emergence of the M-1 phase in $GaNMn_3$ under high pressure in experiment. We find that the Γ_{5g} phase is the ground state of $GaNMn_3$, while the total energies of the Γ_{4g} and M-1 phases are higher by 0.49 meV/f.u. and 164.35 meV/f.u., respectively. This result is consistent with the experimental observations showing the appearance of the Γ_{5g} phase in $GaNMn_3$ at low temperature [21, 22, 24].

The calculated local magnetic moment in the Γ_{5g} and Γ_{4g} phases is about 2.16 μ_B/Mn atom, which is in a qualitative agreement with the experimental and previously calculated values [22,23,38,39]. As expected, the non-collinear AFM configuration leads to a zero net magnetic moment. For the ferrimagnetic M-1 phase, we obtain 2.00 μ_B per Mn atom in the (001) plane and 1.47 μ_B per Mn atom in the (002) plane, resulting in the net magnetic moment of 1.80 μ_B/f.u pointing along the z direction.

Since Γ_{5g} and Γ_{4g} have similar magnetic structures, we first investigate the AHE in these two phases of $GaNMn_3$. Figure 3(a) shows the band structure of the Γ_{5g} phase. Five bands cross the Fermi energy (E_F). These dispersive bands are largely composed of the Mn-3d orbitals. It is seen that in some directions the bands are very close to each other. For example, along the Γ-Z and R-Γ directions, there are nearly degenerate bands.

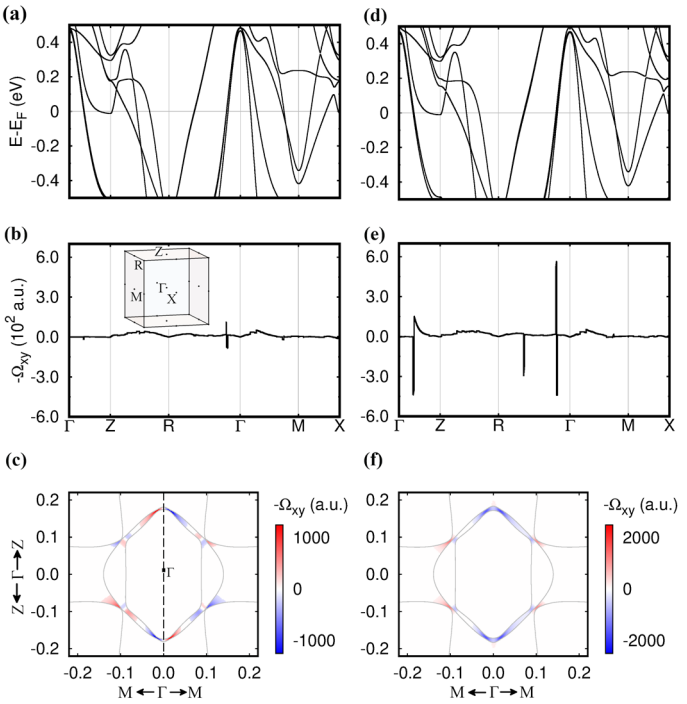

FIG. 3. (a-c) The calculated band structure (a), Berry curvature Ω_{xy} along high symmetry path (b), and the color map of Ω_{xy} in the $(\bar{1}10)$ plane (c) for the Γ_{5g} phase of $GaNMn_3$. (d-f) The calculated band structure (d), Ω_{xy} along high symmetry path (e), and the color map of Ω_{xy} in the $(\bar{1}10)$ plane (f) for the Γ_{4g} phase of $GaNMn_3$. The inset of (b) shows the Brillouin zone. The solid lines and the dashed line in (c) and (f) denote the Fermi surfaces and the mirror plane $M_{\bar{1}10}$.

Figure 3(b) shows the calculated Berry curvature Ω_{xy}. It is seen that there are peaks along the R-Γ direction, which appear, according to Eq. (2), due to the small band separation between the three bands crossing E_F along this direction close to the Γ point (see Fig. 3(a)). Along the Γ-Z direction, the Berry curvature Ω_{xy} is zero within the computation accuracy. This is due to the mirror symmetry $M_{\bar{1}10}$ which holds along this high symmetry direction, resulting in $M_{\bar{1}10}\Omega_{xy}(0,0,k_z) = -\Omega_{xy}(0,0,k_z)$, and hence $\Omega_{xy}(0,0,k_z) = 0$.

In order to demonstrate the odd nature of the Berry curvature under the mirror symmetry $M_{\bar{1}10}$, we plot in Figure 3(c) the color map of Ω_{xy} around the Γ point in the (110) plane, which is perpendicular to the $(\bar{1}10)$ plane. It is seen that hot spots (i.e. regions where the absolute values of the Berry curvature are large) appear around the k-points where the Fermi surfaces of different bands (indicated by solid lines in [Fig. 3(c)]) cross. As is evident from Figure 3(c), Ω_{xy} changes sign with respect to the mirror symmetry transformation $M_{\bar{1}10}$ (reflection with respect to the dashed line in [Fig. 3(c)]). Clearly, integration of the Ω_{xy} over the whole Brillouin zone using Eq. (1) leads to zero AHC

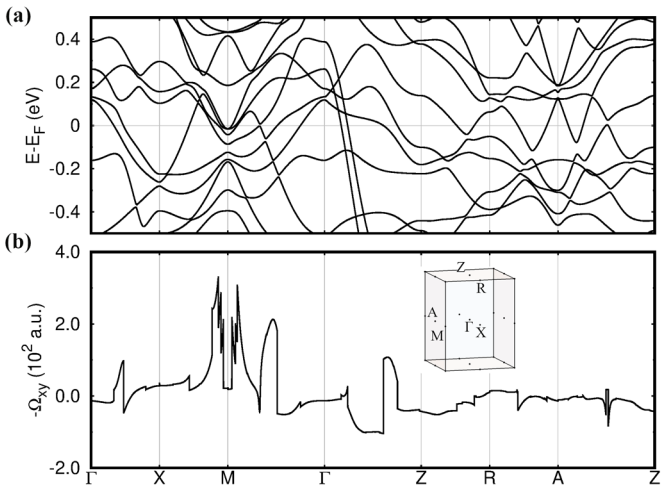

FIG. 4. Calculated band structure (a) and Berry curvature Ω_{xy} (b) of $GaNMn_3$ in the M-1 phase along high symmetry paths in the Brillouin zone. The inset of (b) shows the Brillouin zone.

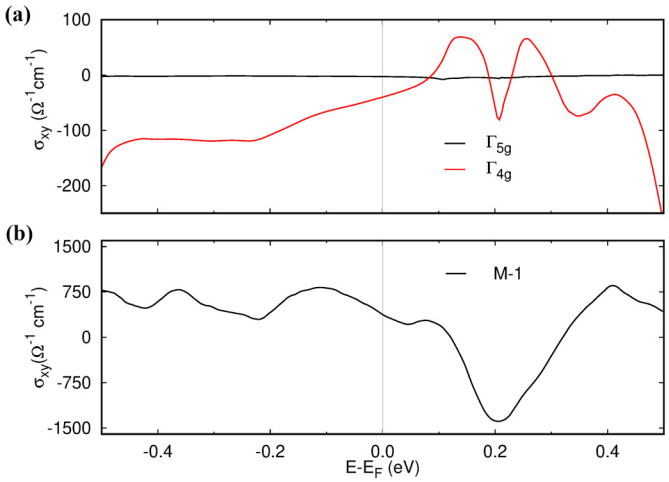

FIG. 5. (a,b) Calculated AHC σ_{xy} as a function of energy for the Γ_{5g} and Γ_{4g} (a) and M-1 (b) phases of $GaNMn_3$.

(within the computational accuracy) for the Γ_{5g} phase. As seen from Fig. 5(a), this property is independent of energy (Fermi energy).

Figure 3(d) shows the band structure of $GaNMn_3$ in the Γ_{4g} phase. The Γ_{4g} phase can be obtained from the Γ_{5g} phase by rotation of all magnetic moments around the [111] axis by 90°, in the absence of SOC the band structure of the two phases should be identical. Thus, the subtle differences in the bands structures in Figures 3(a) and 3(d) are due to SOC. These differences are seen, particularly, along the Γ-Z and Γ-R directions, where there is a slight increase in the band splitting around the Fermi energy.

Figure 3(e) shows the calculated Berry curvature of $GaNMn_3$ in the Γ_{4g} phase and reveals pronounced peaks in Ω_{xy} along the Γ-Z and Γ-R directions. According to the $TM_{\bar{1}10}$ symmetry, Ω_{xy} is an even function of the wave vector $\vec{k}$, i.e. $TM_{\bar{1}10}\Omega_{xy}(k_y, k_x, k_z) = \Omega_{xy}(-k_x, -k_y, -k_z)$. This is reflected in the calculated color map of Ω_{xy} around the Γ point in the (110) plane, which is shown in Figure 3(f). It is seen that the hot spots of Ω_{xy} appear nearly at the same locations as for the Γ_{5g} phase [Fig. 3 (c)]. However, in the Γ_{4g} phase, they are distributed symmetrically and have the same sign, proving that Ω_{xy} is an even function with respect the $TM_{\bar{1}10}$ symmetry transformation. The AHC is calculated by integration of Ω_{xy} according to Eq. (2). Figure 5(a) shows that σ_{xy} is finite as a function of energy and at the Fermi energy $\sigma_{xy} = -40\ \Omega^{-1}cm^{-1}$. Clearly, the difference in the AHC between the Γ_{5g} and Γ_{4g} phases is due to the different magnetic space group symmetry of these phases.

Figure 4(a) shows the calculated band structure of $GaNMn_3$ in the M-1 phase along high symmetry directions in the Brillouin zone. The band structure is more intricate compared to those for the Γ_{5g} and Γ_{4g} phases, because of a larger unit cell and more complex magnetic configuration. The presence on the net magnetic moment breaks time reversal symmetry, which makes the AHC non-zero. Figure 5(b) shows the calculated Berry curvature Ω_{xy} along the high symmetry directions. It is seen that there are number of pronounced broad peaks which are associated with the multiple low dispersive bands around the Fermi energy which are coupled by the spin-orbit interaction. Figure 5(b) shows the calculated AHC as a function of energy in the M-1 phase. At the Fermi energy, $\sigma_{xy} = 377\ \Omega^{-1}cm^{-1}$ which is much larger than the AHC in the Γ_{4g} phase, due to the presence of the net magnetic moment in the M-1 phase. It is notable that σ_{xy} can be strongly enhanced in the M-1 phase by hole doping. For example, at $E = E_F - 0.1$ eV, the calculated value of σ_{xy} is as large as 816 $\Omega^{-1}cm^{-1}$ which is larger than the AHC in Fe (σ_{xy}~700 $\Omega^{-1}cm^{-1}$ [41]).

Similar properties are expected for other antiperovskite compounds, which may exhibit the non-collinear magnetic Γ_{4g} or Γ_{5g} phases. For comparison, we have calculated the AHC of antiperovskites $NiNMn_3$ and $SnNMn_3$, in which the Γ_{4g} phase exists at room temperature [16]. Consistent with the experiment, our calculations find that the Γ_{4g} phase is the ground state for these compounds. The calculated energy difference $\Delta E = E_{5g} - E_{4g}$ is 0.19 meV/f.u. for $NiNMn_3$ and 0.16 meV/f.u. for $SnNMn_3$. Large AHC over 100 $\Omega^{-1}cm^{-1}$ is predicted for the Γ_{4g} phase of $NiNMn_3$ and $SnNMn_3$, as indicated in Table II. The AHE in the Γ_{4g} phase of $NiNMn_3$ has been recently observed experimentally, which confirms our results [42]. Contrary to $GaNMn_3$, we find that the M-1 magnetic configuration is unstable in the $NiNMn_3$ and $SnNMn_3$ antiperovskites.

V. Discussion

Our results demonstrate that in the family of antiperovskite compounds, as represented by $ANMn_3$, the AHC is strongly dependent on the specific magnetic configuration. A significant change in the AHC can be produced by transitions between different magnetic phases. Such transitions can be driven by an external stimulus, provided that the energies of the different non-collinear magnetic phases are engineered to be nearly degenerate.

In experiment, the Γ_{5g} phase is found in the $ANMn_3$ compounds with A = Zn, Ga, and the Γ_{4g} phase is found for A = Ni, Ag, Sn [16]. The M-1 phase can be produced by non-stoichiometry and pressure [23]. These facts imply the sensitivity of the non-collinear magnetic phases to the chemical composition and lattice volume. Recently, monocrystalline $ANMn_3$ films have been successfully grown on different substrates, such as $SrTiO_3$, $BaTiO_3$, and LSAT [43,44]. This opens a possibility to engineer antiperovskite compounds with nearly degenerate energies of the different magnetic phases by proper doping and suitable epitaxial strain produced by the substrate. In particular, the dynamic strain generated by a piezoelectric substrate, such as PMN-PT, can be used to realize the reversible switching between different magnetic phases.

Furthermore, since the AHC is odd under time reversal symmetry, the antiferromagnetic Γ_{4g} phase with a reversed Néel vector (corresponding to 180° rotation of all magnetic moments in the (111) plane) is expected to have AHC of opposite sign. The Néel vector can be switched using a spin transfer torque induced by a spin polarized current [26], and its switching can be detected by the sign change of AHC. This functionality can be engineered by stoichiometry design of the antiperovskite compounds to tune the energy barrier between the two Γ_{4g} states of the opposite Néel vector ($\Delta E = E_{5g} - E_{4g}$) to a lower positive value. These possibilities make the $ANMn_3$ family of materials a promising platform for the AHE based applications of spintronic devices.

VI. Summary

In this work, we have studied the intrinsic AHC in different non-collinear magnetic phases of $GaNMn_3$, as a representative of a broader materials family of antiperovskite compounds $ANMn_3$ (A is a main group element). Based on the symmetry analysis and first-principles DFT calculations, we showed that the nearly degenerate non-collinear AFM Γ_{5g} and Γ_{4g} phases of $GaNMn_3$ have zero and finite AHC, respectively. This difference was explained by the different magnetic space group symmetry of these phases. We also predicted that $GaNMn_3$, in the non-collinear ferrimagnetic M-1 phase, exhibits large AHC which is comparable to the AHC in elemental ferromagnets, such as iron, and calculated the AHC of antiperovskites $SnNMn_3$ and $NiNMn_3$ exhibiting the Γ_{4g} ground state. We argued that by doping and strain it is possible to engineer the $ANMn_3$ compounds where the energy difference between these magnetic phases could be small, so that an external stimulus, such as the dynamic strain or the spin transfer torque could produce switchable magnetic phase transitions. Our work demonstrates that the antiperovskite family of non-collinear magnetic materials is a good platform to realize the multiple AHE states in a single compound, which is promising for novel spintronic applications.

Note added. After the submission of our work, we became aware of two relevant works on the anomalous Hall effect in $ANMn_3$ compounds [42, 45].

Acknowledgments

This research was supported by the National Science Foundation (NSF) through the DMREF (grant DMR-1629270) and E2CDA (grant ECCS-1740136) programs, and the Semiconductor Research Corporation (SRC) through the nCORE program. Computations were performed at the University of Nebraska Holland Computing Center.

APPENDIX

A. Geometry dependence of AHC

The AHC tensor depends on geometry used in transport measurements. TABLE I (Section II) above shows the AHC tensor for $GaNMn_3$ (001) growth orientation corresponding to the standard Cartesian coordinates with x along [100], y along [010], and z along [001] directions. For $GaNMn_3$ (111) sample, the AHC can be measured for a charge current parallel to the Ga-Mn Kagome lattice. Here we show the AHC tensor for a $GaNMn_3$ (111) sample, with x pointing along $[\bar{1}10]$, y along $[\bar{1}\bar{1}2]$ and z along [111] directions. The respective AHC tensor $\sigma_{[111]}$ can be obtained from

$$\sigma_{[111]} = R\,\sigma_{[001]}\,R^{-1} \tag{3}$$

where $\sigma_{[001]}$ is the AHC tensor for $GaNMn_3$ (001) and R represents the respective rotation matrix. The resulting AHC tensors for Γ_{4g} and Γ_{5g} phases are shown in TABLE III, where $\sigma'_{xy} = -68\ \Omega^{-1}cm^{-1}$.

TABLE III. AHC matrix tensors for Γ_{5g} and Γ_{4g} magnetic phases with $\hat{x}||[\bar{1}10]$, $\hat{y}||[\bar{1}\bar{1}2]$ and $\hat{z}||[111]$.

Magnetic Phase	Γ_{5g}	Γ_{4g}
AHC tensor	$\begin{bmatrix} 0 & 0 & 0 \\ 0 & 0 & 0 \\ 0 & 0 & 0 \end{bmatrix}$	$\begin{bmatrix} 0 & \sigma'_{xy} & 0 \\ -\sigma'_{xy} & 0 & 0 \\ 0 & 0 & 0 \end{bmatrix}$

B. *M* and *TM* symmetry operations on the Berry curvature

TABLE IV. Symmetry transformations of wave vector k and Berry curvature Ω.

	Transformation of k	Transformation of $\boldsymbol{\Omega}$
$\boldsymbol{M_{[\bar{1}10]}}$	$M_{[\bar{1}10]}(k_y,k_x,k_z)=(k_x,k_y,k_z)$	$M_{[\bar{1}10]}\Omega_{xy}(k_y,k_x,k_z)=-\Omega_{xy}(k_x,k_y,k_z)$ $M_{[\bar{1}10]}\Omega_{zx}(k_y,k_x,k_z)=-\Omega_{yz}(k_x,k_y,k_z)$ $M_{[\bar{1}10]}\Omega_{yz}(k_y,k_x,k_z)=-\Omega_{zx}(k_x,k_y,k_z)$
$\boldsymbol{M_{[0\bar{1}1]}}$	$M_{[0\bar{1}1]}(k_x,k_z,k_y)=(k_x,k_y,k_z)$	$M_{[0\bar{1}1]}\Omega_{xy}(k_x,k_z,k_y)=-\Omega_{zx}(k_x,k_y,k_z)$ $M_{[0\bar{1}1]}\Omega_{yz}(k_x,k_z,k_y)=-\Omega_{yz}(k_x,k_y,k_z)$ $M_{[0\bar{1}1]}\Omega_{zx}(k_x,k_z,k_y)=-\Omega_{xy}(k_x,k_y,k_z)$
$\boldsymbol{M_{[10\bar{1}]}}$	$M_{[10\bar{1}]}(k_z,k_y,k_x)=(k_x,k_y,k_z)$	$M_{[10\bar{1}]}\Omega_{xy}(k_z,k_y,k_x)=-\Omega_{yz}(k_x,k_y,k_z)$ $M_{[10\bar{1}]}\Omega_{yz}(k_z,k_y,k_x)=-\Omega_{xy}(k_x,k_y,k_z)$ $M_{[10\bar{1}]}\Omega_{zx}(k_z,k_y,k_x)=-\Omega_{zx}(k_x,k_y,k_z)$
$\boldsymbol{TM_{\bar{1}10}}$	$TM_{\bar{1}10}(k_y,k_x,k_z)=(-k_x,-k_y,-k_z)$	$TM_{[\bar{1}10]}\Omega_{xy}(k_y,k_x,k_z)=\Omega_{xy}(-k_x,-k_y,-k_z)$ $TM_{[\bar{1}10]}\Omega_{yz}(k_y,k_x,k_z)=\Omega_{zx}(-k_x,-k_y,-k_z)$ $TM_{[\bar{1}10]}\Omega_{zx}(k_y,k_x,k_z)=\Omega_{yz}(-k_x,-k_y,-k_z)$
$\boldsymbol{TM_{[0\bar{1}1]}}$	$TM_{[0\bar{1}1]}(k_x,k_z,k_y)=(-k_x,-k_y,-k_z)$	$TM_{[0\bar{1}1]}\Omega_{xy}(k_x,k_z,k_y)=\Omega_{zx}(-k_x,-k_y,-k_z)$ $TM_{[0\bar{1}1]}\Omega_{yz}(k_x,k_z,k_y)=\Omega_{yz}(-k_x,-k_y,-k_z)$ $TM_{[0\bar{1}1]}\Omega_{zx}(k_x,k_z,k_y)=\Omega_{xy}(-k_x,-k_y,-k_z)$
$\boldsymbol{TM_{[10\bar{1}]}}$	$TM_{[10\bar{1}]}(k_z,k_y,k_x)=(-k_x,-k_y,-k_z)$	$TM_{[10\bar{1}]}\Omega_{xy}(k_z,k_y,k_x)=\Omega_{yz}(-k_x,-k_y,-k_z)$ $TM_{[10\bar{1}]}\Omega_{yz}(k_z,k_y,k_x)=\Omega_{xy}(-k_x,-k_y,-k_z)$ $TM_{[10\bar{1}]}\Omega_{zx}(k_z,k_y,k_x)=\Omega_{zx}(-k_x,-k_y,-k_z)$

* dfshao@unl.edu
† tsymbal@unl.edu

[1] N. Nagaosa, J. Sinova, S. Onoda, A. H. MacDonald, and N. P. Ong, Anomalous Hall effect. *Rev. Mod. Phys.* **82**, 1539 (2010).

[2] D. Xiao, M.-C. Chang, and Q. Niu, Berry phase effects on electronic properties. *Rev. Mod. Phys*. **82**, 1959 (2010).

[3] Z. Fang, N. Nagosa, K. S. Takahashi, A. Asamitsu, R. Mathieu, T. Ogasawara, H. Yamada, M. Kawasaki, Y. Tokura, and K. Terakura, The anomalous Hall effect and magnetic monopoles in momentum space. *Science* **302**, 92 (2003).

[4] H. Chen, Q. Niu, and A. H. MacDonald, Anomalous Hall effect arising from noncollinear antiferromagnetism. *Phys. Rev. Lett*. **112**, 017205 (2014).

[5] J. Kübler and C. Felser, Non-collinear antiferromagnets and the anomalous Hall effect. *EPL* **108**, 67001 (2014).

[6] S. Nakatsuji, N. Kiyohara, and T. Higo, Large anomalous Hall effect in a non-collinear antiferromagnet at room temperature. *Nature* **527**, 212 (2015).

[7] A. K. Nayak, J. E. Fischer, Y. Sun, B. Yan, J. Karel, A. C. Komarek, C. Shekhar, N. Kumar, W. Schnelle, J. Kübler, C. Felser, and S. P. P. Parkin, Large anomalous Hall effect driven by a nonvanishing Berry curvature in the noncollinear antiferromagnet Mn_3Ge. *Sci. Adv.* **2**, e1501870 (2016).

[8] Y. Zhang, Y. Sun, H. Yang, J. Železný, S. P. P. Parkin, C. Felser, and B. Yan, Strong anisotropic anomalous Hall effect and spin Hall effect in the chiral antiferromagnetic compounds Mn_3X (X=Ge, Sn, Ga, Ir, Rh, and Pt). *Phys. Rev. B* **95**, 075128 (2017).

[9] A. H. MacDonald and M. Tsoi, Antiferromagnetic metal spintronics. *Phil. Trans. R. Soc. A* **369**, 3098 (2011).

[10] T. Jungwirth, X. Marti, P. Wadley, and J. Wunderlich, Antiferromagnetic spintronics. *Nat. Nano.* **11**, 231 (2016).

[11] O. Gomonay, V. Baltz, A. Brataa, and Y. Tserkovnyak, Antiferromagnetic spin textures and dynamics. *Nat. Phys.* **14**, 213 (2018).

[12] M. Seeman, D. Ködderitzsch, S. Wimmer, and H. Ebert, Symmetry-imposed shape of linear response tensors. *Phys. Rev. B* **92**, 155138 (2015).

[13] M. T. Suzuki, T. Koretsune, M. Ochi, and R. Arita, Cluster multipole theory for anomalous Hall effect in antiferromagnets. *Phys. Rev. B* **95**, 094406 (2017).

[14] T. He, Q. Huang, A. P. Ramirez, Y. Wang, K. A. Regan, N. Rogado, M. A. Hayward, M. K. Haas, J. S. Slusky, K. Inumara, H. W. Zandbergen, N. P. Ong, and R. J. Cava, Superconductivity in the non-oxide perovskite $MgCNi_3$. *Nature* **411**, 54 (2001).

[15] K. Kamishima, T. Goto, H. Nakagawa, N. Miura, M. Ohashi, N. Mori, T. Sasaki, and T. Kanomata, Giant magnetoresistance in the intermetallic compound Mn_3GaC. *Phys. Rev. B* **63**, 024426 (2000).

[16] D. Fruchart and E. F. Bertaut, Magnetic studies of the metallic perovskite-type compounds of manganese. *J. Phys. Soc. Jap.* **44**, 781 (1978).

[17] T. Kaneko, T. Kanomata, and K. Shirakawa, Pressure effect on the magnetic transition temperatures in the intermetallic compounds Mn_3MC (M = Ga, Zn and Sn). *J. Phys. Soc. Jap.* **56**, 4047 (1987).

[18] K. Takenaka, M. Ichigo, T. Hamada, A. Ozawa, T. Shibayama, T. Inagaki, and K. Asano, Magnetovolume effects in manganese nitrides with antiperovskite structure. *Sci. Tech. Adv. Mat.* **15**, 015009 (2014).

[19] T. Tohei, H. Wada, and T. Kanomata, Negative magnetocaloric effect at the antiferromagnetic to ferromagnetic transition of Mn_3GaC. *J. Appl. Phys.* **94**, 1800 (2003).

[20] B. S. Wang, P. Tong, Y. P. Sun, X. Luo, X. B. Zhu, G. Li, X. D. Zhu, S. B. Zhang, Z. R. Yang, and W. H. Song, Large magnetic entropy change near room temperature in antiperovskite $SnCMn_3$, *EPL* **85**. 47004 (2009).

[21] D. Matsunami, A. Fujita, K. Takenaka, and M. Kano, Giant barocaloric effect enhanced by the frustration of the antiferromagnetic phase in Mn_3GaN. *Nat. Mater.* **14**, 73 (2015).

[22] E. F. Bertaut, D. Fruchart, J. P. Bouchaud, and R. Fruchart, Diffraction neutronique de Mn_3GaN. *Solid St. Commun.* **6**, 251 (1968).

[23] K. Shi, Y. Sun, J. Yan, S. Deng, L. Wang, H. Wu, P. Hu, H. Lu, M. I. Malik, Q. Huang, and C. Wang, Baromagnetic effect in antiperovskite $Mn_3Ga_{0.95}N_{0.94}$ by neutron powder diffraction analysis. *Adv. Mater.* **28**, 3761 (2016).

[24] K. Takenaka, T. Inagaki, and H. Takagi, Conversion of magnetic structure by slight dopants in geometrically frustrated antiperovskite Mn_3GaN. *Appl. Phys. Lett.* **95**, 132508 (2009).

[25] S. Likubo, K. Kodama, K. Takenaka, H. Takagi, and S. Shamoto, Magnetovolume effect in $Mn_3Cu_{1-x}Ge_xN$ related to the magnetic structure: Neutron powder diffraction measurements. *Phys. Rev. B* **77**, 020409 (2008).

[26] H. Fujita, Field-free, spin-current control of magnetization in non-collinear chiral antiferromagnets, *Phys. Stat. Solidi (RRL)* **11**, 1600360 (2017).

[27] M. Gradhand, D. V. Fedorov, F. Pientka, P. Zahn, I. Mertig, and B. K. Györffy, First-principle calculations of the Berry curvature of Bloch states for charge and spin transport of electrons. *J. Phys.: Condens. Matter* **24**, 213202 (2012).

[28] D. Vanderbilt, Soft self-consistent pseudopotentials in a generalized eigenvalue formalism. *Phys. Rev. B* **41**, 7892 (1990).

[29] P. Giannozzi *et al*., QUANTUM ESPRESSO: A modular and open-source software project for quantum simulations of materials. *J. Phys.: Condens. Matter* **21**, 395502 (2009).

[30] J. P. Perdew, K. Burke, and M. Ernzerhof, Generalized gradient approximation made simple. *Phys. Rev. Lett.* **77**, 3865 (1996).

[31] F. D. Murnaghan, The compressibility of media under extreme pressures. *Proc. Natnl. Aca. Sci. USA* **30.9,** 244 (1944).

[32] M. B. Nardelli, F. T. Cerasoli, M. Costa, S. Curtarolo, R. De Gennaro, M. Fornari, L. Liyanage, A. Supka, and H. Wang, PAOFLOW: A utility to construct and operate on *ab-initio* Hamiltonians from the projections of electronic wavefunctions on atomic orbital bases, including characterization of topological materials. *Comp. Mat. Sci.* **143**, 462 (2017).

[33] L. A. Agapito, A. Ferretti, A. Calzolari, S. Curtarolo, and M. B. Nardelli, Effective and accurate representation of extended Bloch states on finite Hilbert spaces. *Phys. Rev. B* **88**, 165127 (2013).

[34] L. A. Agapito, S. Ismail-Beigi, S. Curtarolo, M. Fornari, and M. B. Nardelli, Accurate tight-binding hamiltonian matrices from *ab-initio* calculations: Minimal basis sets. *Phys. Rev. B* **93**, 035104 (2016).

[35] J. Železný, https://bitbucket.org/zeleznyj/linear.

[36] K. Momma, and F. Izumi, VESTA: a three-dimensional visualization system for electronic and structural analysis. *J. Appl. Crystal.* **41**, 653 (2008).

[37] T. Williams, C. Kelley, H. B. Broker, J. Campbell, R. Cunningham, D. Denholm, E. Elber, R. Fearick, C. Grammes, and L. Hart, Gnuplot 4.5: An interactive plotting program, 2011. *URL http://www. gnuplot. Info* (2017).

[38] P. Lukashev, R. F. Sabirianov, and K. Belashchenko, Theory of piezomagnetic effect in Mn-based antiperovskites. *Phys. Rev. B* **78**, 184414 (2008).

[39] J. Zemen, Z. Gercsi, and K. G. Sandeman, Piezomagnetism as a counterpart of the magnetovolume effect in magnetically frustrated Mn-based antiperovskite nitrides. *Phys. Rev. B* **96**, 024451 (2017).

[40] D.-F. Shao, G. Gurung, T. R. Paudel, and E. Y. Tsymbal, Electrically reversible magnetization at the antiperovskite/ perovskite interface. *Phys. Rev. Materials* **3,** 024405 (2019).

[41] Y. Yao, L. Kleinman, A. H. MacDonald, J. Sinova, T. Jungwirth, D. Wang, and Q. Niu, First-principles calculation of anomalous Hall conductivity in ferromagnetic bcc Fe. *Phys. Rev. Lett.* **92**, 037204 (2004).

[42] D. Boldrin, I. Samathrakis, J. Zemen, A. Mihai, B. Zou, B. Esser, D. McComb, P. Petrov, H. Zhang, and L. F. Cohen, The anomalous Hall effect in non-collinear antiferromagnetic Mn_3NiN thin films. ArXiv:1902.04357 (2019).

[43] D. Boldrin, A. P. Mihai, B. Zou, J. Zemen, R. Thompson, E. Ware, B. V. Neamtu, L. Ghivelder, B. Esser, D. W. McComb, P. Petrov, and L. F. Cohen, Giant piezomagnetism in Mn_3NiN. *ACS Appl. Mater. Interfaces* **10**, 18863 (2018).

[44] C. X. Quintela, K. Song, D.-F. Shao, L. Xie, T. R. Paudel, N. Campbell, M. S. Rzchowski, E. Y. Tsymbal, S.-Y. Choi, and C.B. Eom, Epitaxial antiperovskite/perovskite heterostructures for materials design. *Submitted paper*.

[45] X. Zhou, J. -P. Hanke, W. Feng, F. Li, G.-Y. Guo, Y. Yao, S. Blügel, and Y. Mokrousov, Spin-order dependent anomalous Hall effect and magneto-optical effect in the noncollinear antiferromagnets Mn_3XN with X=Ga, Zn, Ag, or Ni. *Phys. Rev.* B 99, 104428 (2019).